Research Article | Vol. 14, No. 12 / 1 Dec 2024 / Optical Materials Express 2830

Optical Materials EXPRESS

Polarization insensitive electrically reconfigurable meta-lens for the 2 µm wavelength

Md. Asif Hossain Bhuiyan,[1,2,3] Purbayan Das,[1,2] and Sajid Muhaimin Choudhury[1,*]

[1] *Department of Electrical and Electronic Engineering, Bangladesh University of Engineering and Technology, Dhaka 1205, Bangladesh*
[2] *Department of Computer Science and Engineering, BRAC University, Dhaka 1212, Bangladesh*
[3] *Department of Electrical and Computer Engineering, Boise State University, 1910 University Drive, Boise, Idaho 83725, USA*
[*] *sajid@eee.buet.ac.bd*

Abstract: The conventional fiber communication band of 1.55 µm is reaching its limit attributable to the escalation in bandwidth requirements for high-speed and bulk data transmission. Researchers are exploring a 2 µm waveband for its higher capacity and low attenuation as a solution for the next generation communication technologies. Accordingly, here we report an optically engineered metasurface for this waveband for fiber coupling or lensing. The structure is polarization-insensitive and dynamically tunable between its reflective (OFF) and transmissive (ON) modes. For tunability, we incorporate a novel phase change material In_3SbTe_2 (IST) for its faster, non-volatile, and reversible metallic-to-insulator phase transition. The integration of indium tin oxide (ITO) as a micro-heater to electrically modulate the light by altering the phase of IST provides the device with additional functionality for point-of-care applications. Using the finite-difference-time-domain (FDTD) technique, we have achieved a modulation depth of 90%. The focusing efficiency is as high as 76% and the ON-OFF switching ratio of the optimized lens is 26 dB. The multilayer insertion of thin IST ensures uniform phase transition with switching energy as low as 232.98 nJ/µm^2. Thus, with remarkable performance at 2 µm and dynamic multifunctionality, our proposed device will revolutionize the upcoming telecommunication technologies and beyond.

1. Introduction

The ever-expanding demand for high-speed and secured data transmission has led to continuous innovation in optical fiber communication. Although the existing 1.55 µm fiber technologies are dealing with this ongoing demand by introducing time, polarization, and wavelength multiplexing or spectrally efficient coding [1], data compression [2], and parallel connections [3], the 2 µm optical communication band has emerged as a promising frontier due to its higher bandwidth capacity and reduced signal attenuation [4]. Accordingly, researchers are bringing breakthroughs in optical communication technology by engineering materials and nanostructure for this waveband. Previously, P. J. Roberts et. al. [5] developed a low loss (0.13 dB/km) hollow-core fiber, and Eoin Russell et al. [6] proposed a fiber amplifier for this optical band. Moreover, 2 µm laser sources such as Tm:YLF, Tm:Lu_2O_3, Ho:YAG, and Ho:YLF are commercially available [7]. Si [8] and phase-change-material (PCM) [9] based optical modulators for this spectral band have also been studied. Apart from these optical components, fiber-integrated metasurfaces for phase, amplitude, and polarization control, beam convergence, optical coupling, and axially shifted imaging have lately drawn the attention of researchers for 'all-in-fiber' applications [10]. Additionally, metasurfaces with multifunctionality such as transmittance modulated lensing

#540435 https://doi.org/10.1364/OME.540435
Journal © 2024 Received 9 Sep 2024; revised 25 Oct 2024; accepted 29 Oct 2024; published 11 Nov 2024

Optical Materials EXPRESS

[11], focusing and beam steering [12], and beam splitter: from a Gaussian to a Bessel and a helical beam [13] have been rigorously investigated in recent times. However, a reconfigurable metasurface for lensing or beam steering for the 2 μm spectral range has yet to be reported.

Currently, PCM has been the primary choice for reconfigurable photonics: varifocal metalens [14], switchable waveplates [15], beem steering [16], plasmonic absorbers [17], intensity modulators [18], displays [19], memory elements [20], camouflage [21], thermal emitters [22], and many more. PCM is suitable for optical manipulation because of the pronounced contrast in optical properties between its chemically stable phases and the realization of ultra-fast and reversible phase transition with electrical, thermal, or optical stimuli. These devices regulate their optical characteristics by exploiting either non-volatile chalcogenide PCMs (GeTe [23,24], $Ge_2Sb_2Te_5$ [25,26], $Ge_2Sb_2Se_4Te_1$ [27,28], Sb_2Te_3 [29,30], Sb_2S_3 [31,32], Sb_2Se_3 [33,34], In_3SbTe_2 [35]) or volatile metal oxides: vanadium oxides (VO_2) [36], titanium oxides (TiO_2) [37], iron oxide (Fe_3O_4) [38], lanthanum cobaltite ($LaCoO_3$) [39], niobium dioxide (NbO_2) [40] etc. VO_2 shows an insulator-to-metallic phase transition by altering the sign of the real part of its permittivity upon temperature variation [41]. IST shows a similar phase transition from amorphous (insulator) to crystalline (metallic) for a broad infrared (IR) range in contrast to other chalcogenide PCMs and an additional feature of non-volatility makes it a promising candidate for IR modulation [42]. Unlike metavalent bonds in most PCMs, the metallic bonds during the crystalline phase elevate IST's potential as an ultrathin absorber [43]. Moreover, thermal radiation modulation [44], nanolight manipulation [45,46], and infrared beam shaping [47] have been experimentally investigated upon non-volatile phase transitions of IST.

In this paper, we design a metasurface for lensing at 2 μm with an enticing feature of electro-optic intensity modulation utilizing the unique properties of IST. The metasurface consists of spatially distributed phase modulators, covering a phase range of 2π. We have accomplished the propagation phase modulation by incorporating dielectric nanopillars of varied diameters, which act as waveguides for different effective refractive indices and add distinct phases to the transmitted wave. Due to the lateral symmetry of the cylindrical nanopillars, the metasurface is polarization insensitive and works for both linearly polarized (LP) and circularly polarized (CP) lights. Additionally, we have incorporated multiple layers of IST below the nanopillars to control the intensity of transmitted light. Thus, by applying appropriate voltages to the ITO layers, we can alter the phase of IST and the transmittance of the metalens. For the amorphous state of IST, more than 90% transmittance is achieved and during the crystalline phase, less than 18% transmittance is observed. Due to the multilayer design and the independent control over the layers, the device provides four different transmittance magnitudes, suitable for multilevel memory applications. While most of the PCM-based switchable metalenses are proposed as proof of concept, lacking the real-life feasibility–transfiguration through thermal annealing [48], we incorporated a transparent conductive material (ITO) [49] as a micro-heater for active phase alteration of IST through joule heating. Applying different bias voltages to the ITO, the temperature has been controlled to revert the phase of IST. Thus, this electrically configurable multifunctional metadevice will find its way into 'point-of-care' applications for 2 μm fiber communication or memory application.

The organization of this article is as follows: a structural description underscoring the optimization of the unit cells to achieve the required phase and amplitude profile for lensing, and an electro-thermal analysis of the structure to illustrate the switching mechanism. Next, the device's focusing capability and intensity modulation have been investigated by demonstrating the tunable focusing of the metalens with the unit cells placed radially maintaining the required phase gradient. Finally, we analyze the polarization insensitivity of the design by comparing the focusing modulation of the metalens for the LP and the CP light.

Optical Materials EXPRESS

2. Structural design

Figure 1(a) illustrates the graphical representation of the device functionality. With this metalens, we can modulate the intensity of the focused light through the joule heating and the subsequent phase transition of the PCM. Figure 1(b) shows the unit cell of metastructure detailing the structural parameters and the materials. The unit cell comprises an AlN nanopillar atop a base of three SiO_2-IST-ITO trilayers on SiO_2 substrate. The nanopillar serves as a waveguide with a high refractive index (2.16) and a low extinction coefficient ($\sim 10^{-5}$) to provide necessary phase delays while minimizing transmission losses [50]. The propagation phase shift through a nanopillar can be approximated by $\frac{2\pi n_{eff} h}{\lambda}$, where n_{eff} is the effective refractive index of the medium, λ is the wavelength, and h is the propagation distance of the light i.e. the height of a nanopillar. Here, the diameter of the nanopillar is varied to achieve the required n_{eff} as the unit cells containing nanopillars of different diameters contribute different phase delays to the transmitted light covering a 2π range. Additionally, we have incorporated IST to modulate the intensity of the transmitted light by altering its chemical structure to switch between its amorphous (dielectric) and crystalline (metallic) phases through joule heating. We avoid heating the IST layers with electrical current directly flowing through them to mitigate the non-uniform joule heating [51], because, in that case, the crystalline path formed initially in the IST has a lower resistance and the current avoids the surrounding amorphous path causing non-uniform heating. To tackle this issue, we utilize an ITO layer adjacent to an IST layer as a micro-heater to facilitate uniform heating. The base of the metasurface is extended to connect the ITO layers with the external circuit. The circular metasurface resides on a rectangular base etched stepwise for contacts on ITO as shown in Fig. 1(c) (top view) and 1(d) (cross-sectional view). This approach is analogous to the indirect heating method demonstrated by Sajiad et al. [51], where the authors utilized a microheater composed of a tungsten (W) layer deposited on a hafnia (HfO_2)-coated Si substrate to thermally modulate the phase of $Ge_2Sb_2Te_5$ (GST). Provided that ITO is a transparent conducting oxide (TCO) with a refractive index close to unity (0.95) and an extinction coefficient of 0.1 at 2 μm [52], a thin layer of ITO does not interrupt the incident light and its conductive nature generates heat when a current flows through it. Depending on the materials of the waveguide or the fiber the metalens will be integrated with, refractive index grading can be accomplished at the bottom of the lens to reduce the reflection from the interface and this analysis is beyond the scope of this article.

Table 1 summarizes all the structural parameters. Here, t_{SiO_2}, t_{IST}, t_{ITO}, and t_{sub} denote the thicknesses of SiO_2, IST, ITO, and substrate layers respectively. The nanopillar has a height of h and a diameter of D, which varies from 0 nm to 730 nm.

Table 1. Structural parameters and their dimensions

Parameter	Dimension (nm)
P	800
h	2500
t_{SiO_2}	500
t_{IST}	8
t_{ITO}	20
t_{sub}	5000

Optical Materials EXPRESS

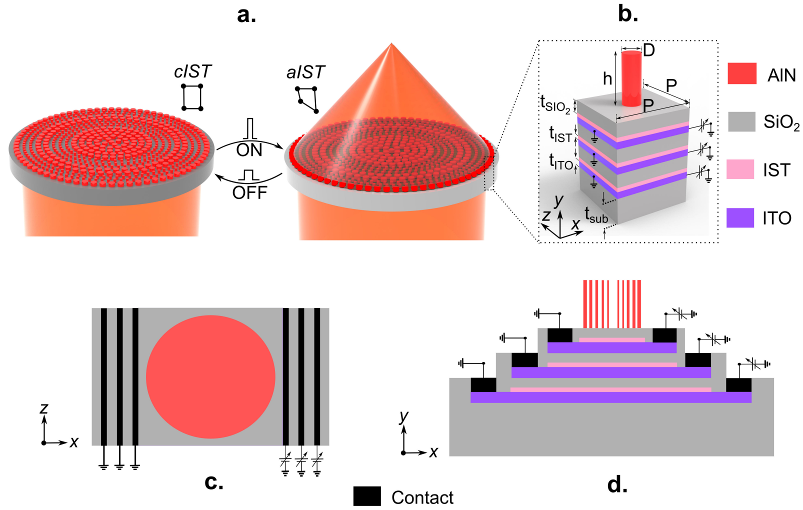

Fig. 1. (a) Schematic view of our proposed switchable metalens. Incident light is mostly reflected during the crystalline phase of IST (cIST) illustrating the OFF state. A high-voltage short-duration pulse to the ITO can heat the cIST to its melting point and turn it into amorphous (aIST). The device becomes transmissive in this state and focusing occurs at the focal point. We can turn it OFF again by applying another low-voltage pulse to crystallize the IST. (b) The unit cell of the metastructure is shown with all the structural parameters. Different colors in the cell represent different materials. The variable voltage sources denote the joule heating circuitry. (c) Schematic top view of the device facilitating the electrical inputs. The red circle represents the whole phase-graded metasurface and the extended base with contacts on ITO layers is for applying electrical signals. (d) Cross-sectional view of the device showing electrical contacts.

3. Methodology and results

The section is divided into three parts: the required transmittance and the phase profile of the unit cells for lensing have been investigated using the FDTD technique; an electro-thermal analysis for the insulator-metallic phase transition of the PCM by joule heating to modulate transmittance is shown; and finally, an FDTD analysis of the phase-graded metasurface for lensing is discussed.

3.1. Optical response of the unit cell

To design a focusing metasurface, the transmission phase contributions of the meta-atoms or the unit cells should preferably cover the 2π phase range. Different phase contributions can be achieved by tailoring the effective refractive indices of the meta-atoms. We have varied the diameter of the nano-pillars to achieve the effective refractive index for the required phase profile. The lateral symmetry in the nanopillars makes the structure polarization insensitive. Additionally, PCM layers are incorporated to modulate the intensity of the transmitted light and here, we utilize IST as PCM due to its non-volatile and reversible metallic(crystalline)-to-insulator(amorphous) phase transition. In the amorphous state (aIST), the real part of its permittivity is positive allowing a high transmittance (~90%), maintaining the required phase profile. We denote this as the ON state of our device. The real part of the permittivity becomes negative during the crystalline phase of IST (cIST) evincing metallic properties. In this state, light is mostly reflected by cIST layers, and the transmittance falls (<18%) manifesting the OFF state of the metastructure. Instead of using a thick layer of IST, we have introduced three thin layers of IST, filling the gaps with SiO_2, to reflect more light during the OFF state. Apart from these two antipodal states, the structure can accommodate two additional intermedial states resulting from the independent control over the IST layers. Instead of altering the phase of the three amorphous IST layers altogether, we can crystallize any one or two IST layers resulting in two different transmittance levels (~ 43% and ~ 67%) between the ON and the OFF states. Thus, the structure serves as a four-state optical memory. Figure 2(a) illustrates the transmittance and phase profile of the device for LP and CP light for both ON and OFF states. It is worth noting that the relative phase profile depends only on the diameters of the nanopillars. The permittivity profiles of aIST and cIST are shown in Fig. 2(b) and 2(c) respectively.

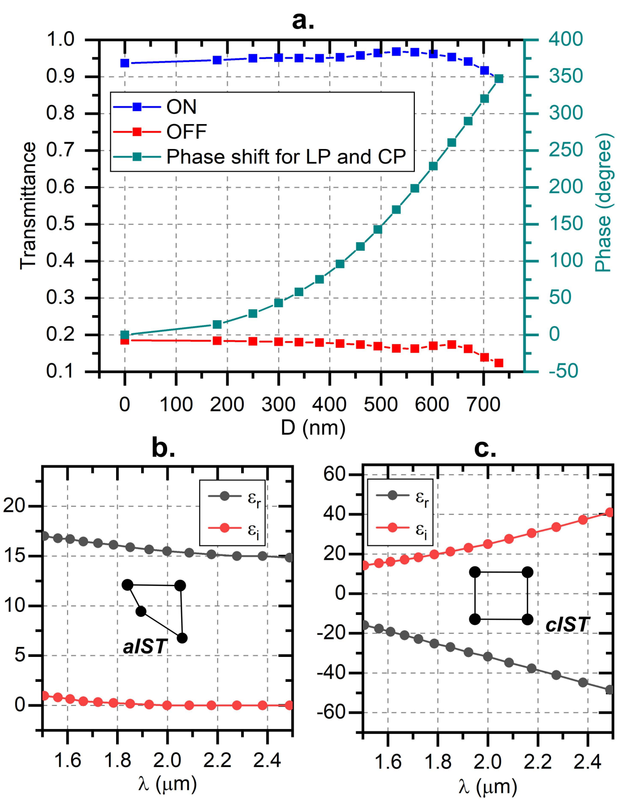

Fig. 2. (a) Transmittance and phase profile during ON and OFF state of the metastructure upon incidence of LP and CP light for different diameters of nanopillars. Real part (ϵ_r) and imaginary part (ϵ_i) of electric permittivity of (b) aIST and (c) cIST plotted as a function of wavelength (λ).

For the FDTD analysis of the unit cell, we set the periodic boundary condition in the x and z directions with a period of 800 nm and a PML condition in the y directions. Additionally, we have used the mesh size of 1 nm for IST and ITO layers. The structure has been illuminated by plane wave sources with a center wavelength of 2 µm. The injection plane is zx and the direction of injection is +y. A single source is used with polarization along the x-axis to study the optical response of the structure for LP light while two LP sources are used to design the CP light source: one is x-polarized and the other is y-polarized. Depending on the phase of the y-polarized source (+90° or − 90°), the resultant injected light becomes either left or right circularly polarized (LCP/RCP). A 2D y-normal monitor is placed above the structure to record the transmittance and phase of the propagated light.

Optical Materials EXPRESS

To analyze the OFF state dynamics, we have examined the cross-sectional electric field profile of the structure along the xy plane. It is evident from the electric field distribution, shown in Fig. 3(a), that light is barely absorbed which mitigates the unnecessary heating issue during the OFF state. Three cIST layers reflect the incident light mostly, allowing very low transmittance. We observe the dielectric scattering of the leaky modes around the nanopillar transmitted through the structure during the OFF state [53]. Besides, the high transmittance during the ON state mitigates the unwanted heating upon absorption. The ON-OFF modulation depth (MD), defined as the difference of transmittance during the ON and OFF state, is achieved as high as 80.36% for three multilayers. Figure 3(b) manifests that increasing the number of layers improves overall performance; however, the energy budget to turn ON/OFF the device increases drastically, which has been discussed later.

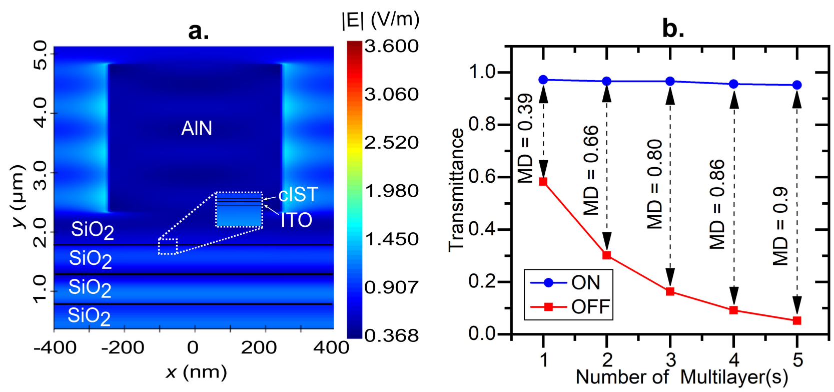

Fig. 3. (a) Electric field profile along the xy plane when the device is OFF. The structure highly reflects the incident light to the bottom. (b) Modulation depths (MDs) of the device for different numbers of SiO_2-IST-ITO multilayers.

3.2. Electro-thermal analysis

We have incorporated ITO as a micro-heater just below the IST for joule heating to achieve electrical control over transmittance modulation. ITO is a very stable conductive oxide, preferable for high-temperature applications such as phase transition of IST [54]. The crystallization of IST occurs when its temperature reaches the glass transition temperature (T_g) of 553.16 K [55]. A low-voltage long-duration voltage pulse and the subsequent electrical current through ITO can heat IST gradually to exceed the temperature T_g. As the thin IST layer resides on ITO, uniform heating and homogeneous crystallization are predictable. For amorphization, IST needs to be heated over its melting point (T_m = ~900 K) followed by a quick cooling with a minimum cooling rate of 1 K/ns [17]. A high-voltage short-duration voltage pulse is employed to melt the IST momentarily. The thick SiO_2 on IST ensures the necessary cooling rate by absorbing heat. Rapid melting and immediate cooling turn IST into an amorphous solid.

To investigate the phase transformation of IST numerically, we have employed the joule heating study of COMSOL Multiphysics. The study utilizes two physics: electrical current and heat transfer in solids. A 15 μm × 15 μm tri-layer structure of SiO_2-IST-ITO was built with their corresponding thicknesses for this analysis. For electrical input, two opposite faces of the ITO are set as voltage terminals, and the other boundaries are set as electric insulators to keep the current confined to the ITO layer. The multiphysics couples the generated heat from ITO due to electrical current to the heat transfer module which analyzes the heat flux from the heat source i.e. the ITO layer. The IST and the SiO_2 layers get heated from the ITO mostly by the conductive heat transfer. All the outer surfaces of the structure were set to surface-to-ambient-radiation

Optical Materials EXPRESS

boundary condition in addition to a convective heat flux for free convection of air (convective heat transfer coefficient, $h = 5$ W/m^{2}K). The initial temperature of the structure was set to 293.16 K. The thermal conductivity of SiO_2 used is ~ 1.3 W/mK [56]. The electrical and thermal conductivities of ITO are interrelated and approximated as 3×10^4 S/m and 4 W/mK respectively for a 20 nm thick ITO layer within the temperature range of interest [54,57]. As the electrical current is confined to the ITO layer, we have omitted the electrical conductivity of IST from this study. The thermal conductivities of aIST and cIST can be estimated as 0.4 W/mK and 0.7 W/mK respectively [55]. Figure 4 demonstrates the joule heating and the corresponding phase transition of an IST layer. In Fig. 4(a), a square voltage pulse having 24 V amplitude and 100 ns pulsewidth has been applied to the ITO and the average temperature of the IST layer gradually reaches T_g manifesting its crystallization after ~ 100 ns. Another 60 V square pulse for 20 ns re-amorphizes the IST by fleetingly melting it followed by a rapid cooling as depicted in Fig. 4(b). In both cases, we took the temperatures beyond the requirements for a uniform and complete phase transition. If the phase transition of all the IST layers is accomplished concurrently, the device takes 15 ns and 80 ns to be turned ON (t_{ON}) and OFF (t_{OFF}) respectively, referred to Fig. 4. We have estimated the required switching time by the time the temperature of each IST layer reaches the necessary threshold from the instance the heating current starts to flow resulting from the applied voltage pulse. Thus, the switching frequency of the device is as high as 10.53 MHz. The switching frequency between any two of the four distinct transmittance states is the same as we can crystallize or amorphize the IST layers either independently or simultaneously. Total electrical energy requirements to turn the device ON and OFF are 43.2 nJ/μm^2 and 34.46 nJ/μm^2 per multilayer respectively. There is a trade-off between the energy budget and the modulation depth and we have optimized our design with three multilayers. Thus, the optimized device has 80% MD with an energy budget of 232.98 nJ/μm^2. Even shorter pulses with higher voltages can provide the necessary temperature; however, the maximum temperature of the PCM near the heater goes way beyond. In this case, when we try to crystallize the IST by taking its temperature above T_g, a portion of IST above the heater melts and stays in the amorphous state as the maximum temperature hits T_m. In contrast, a designer can significantly reduce the voltages for joule heating by involving longer pulses (~ μs). Effective switching is possible as long as the required energy is provided. However, reliable numerical analysis with such longer pulses is computationally demanding.

Figures 5(a) and 5(b) demonstrate the temperature profiles across one micro-heater unit encapsulated by two SiO_2 layers when the temperature is maximum during the crystallization and the amorphization of the PCM respectively. The profiles have Gaussian shapes with a peak at the ITO heater and gradually fall to a lower temperature near other ITO-SiO_2 interfaces. The temperature distribution is wider during the crystallization process than that of amorphization, because the former utilizes a longer voltage pulse and the heat conduction occurs for a longer time. However, as we have incorporated a 500 nm SiO_2 layer, thick enough to thermally isolate one IST layer from another, the electrical heating of a particular IST layer does not interrupt the phase of other IST layers upon phase transition.

3.3. Analysis of the phase-graded metasurface

Metalenses add necessary phase delays to the light waves transmitted from different points on the metasurface, allowing constructive interference to occur at the focus despite traveling different distances by the light waves. Equation (1) relates different points on the metasurface with their required phase contributions.

$$\psi(r) = -\frac{2\pi}{\lambda}(\sqrt{r^2 + F^2} - F) + 2m\pi \tag{1}$$

Here, ψ is the required phase contribution from a point on the metasurface, r is the radial distance of the point from the center of the metalens, λ is the wavelength of light, F is the focal

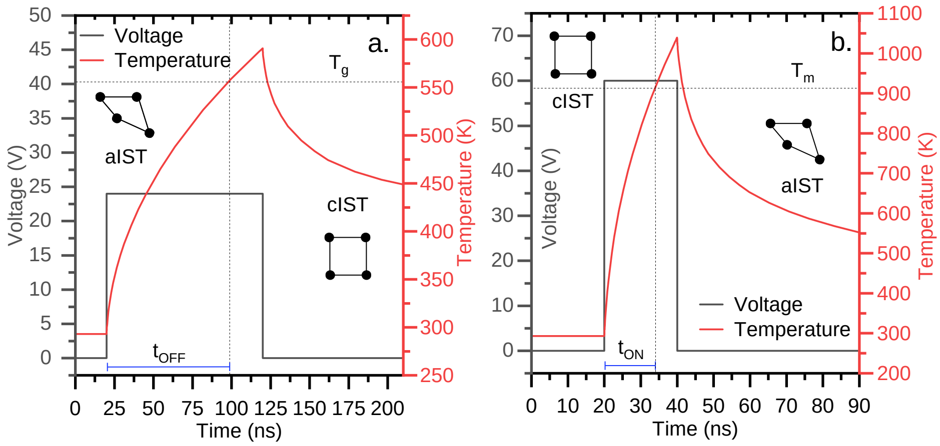

Fig. 4. The applied voltage pulses to the ITO layer and the corresponding variation in the average temperatures of the IST layer with time for (a) crystallization and (b) re-amorphization of the IST. The vertical dashed line in (a) signifies the instant when the average temperature exceeds the glass transition temperature (T_g), depicted as the horizontal dashed line and the crystallization commences. In (b), the vertical dotted line indicates that the melting initiates as the temperature hits the melting point (T_m), specified as the horizontal dashed line. In both cases, we have exceeded the necessary temperature for a uniform and complete phase transformation. Moreover, the durations to turn the device OFF (t_{OFF}) and ON (t_{ON}) have been outlined in (a) and (b) respectively.

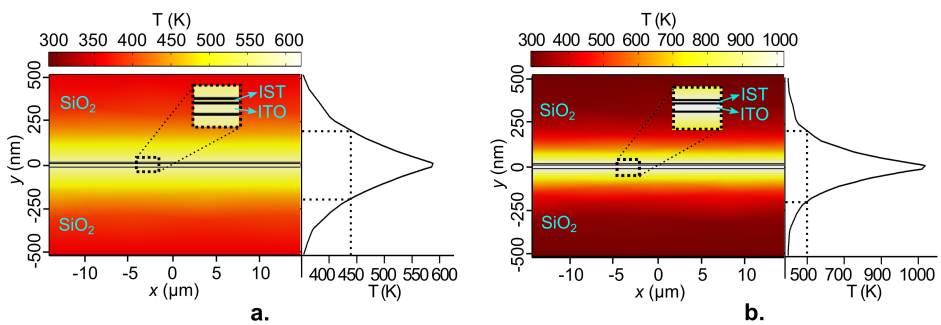

Fig. 5. Temperature (T) distribution across one micro-heater unit when the system temperature is maximum during (a) crystallization and (b) amorphization processes. For the crystallization process, the temperature does not exceed 440 K, 200 nm apart from the micro-heater in either direction as depicted by the dotted lines. Similarly, as denoted by the dotted lines in (b), the temperature drops under 500 K within 200 nm of the micro-heater during the amorphization process manifesting the independent phase transition control over the PCM layers.

length, and m is an arbitrary integer to map the phase in the range of 0 to 2π. For this work, $\lambda = 2$ µm and $F = 60$ µm. A 16-level phase quantization has been utilized that corresponds to 16 different diameters of the nanopillars, summarized in Table 2. The determined phases are matched to the nearest quantization level, and the nanopillars are positioned on the metasurface correspondingly to satisfy the phase criteria for focusing.

Figure 6(a) illustrates the mechanism of placing the unit cells, each containing a single nanopillar, to create the focusing metasurface. Depending on the distance from the center of

Optical Materials EXPRESS

Table 2. Dataset of the relative phases corresponding to the nanopillar diameters

Phase (deg)	D (nm)	Phase (deg)	D (nm)
0	0.00	142.758	494.00
13.9515	180.00	169.674	530.00
28.8521	250.00	198.754	566.00
43.1426	300.00	228.883	602.00
58.1045	340.00	260.717	638.00
75.2658	380.00	289.873	670.00
96.2522	420.00	320.209	702.00
119.842	460.00	347.603	730.00

the metalens, the necessary phase is found from 1 and from that phase value, Table 2 translates the diameter of the nanopillar to be placed. In Fig. 6(a), the same color-coded unit cells (square boxes) are equidistant from the center of the lens and comprise identical nanopillars with the same phase contribution. For example, gray cells are $r = r_1 = 800$ nm (period of the unit cell) apart from the center. Their relative phase contribution, calculated using 1, is -0.95 deg, for which 0 is the closest quantization level in the discretized phase dataset in Table 2. Thus, the gray cells do not contain any nanopillar ($D = 0$). In a similar manner, red ($r = 2r_1$), orange ($r = \sqrt{2}r_1$), and green cells ($r = \sqrt{5}r_1$) are placed with correlated nanopillars according to Table 2 and is continued until $r = 15.5\mu m$ ($= R$, the radius of the metalens).

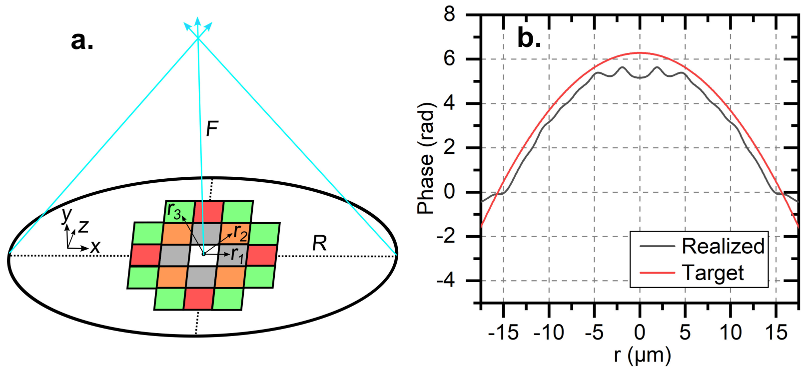

Fig. 6. (a) Artistic view of placing the unit cells to construct the metalens. Here, the same color-coded cells are identical in terms of the radial distance and the phase contribution. (b) Comparison between the realized phase profile () of the transmitted light through the metastructure with the target phase (red).

We have utilized the three-dimensional FDTD technique to investigate the output phase profile for the ON state of the device using Lumerical FDTD Solutions. A 2D field monitor has been placed just above the nanopillars for this. Owing to the symmetry of the lens, we have used symmetrical and anti-symmetrical boundary conditions along the z and the x-axes respectively for x-polarized incident light. PMLs are used in y directions. For circularly polarized incident light, we have used PMLs in all directions. The realized phase profile along x, plotted in Fig. 6(b), exerts an acceptable coherence with the target phase profiles.

The electromagnetic field profile recorded in the monitor is then projected along the +ve y direction to find the focal plane. A satisfactory focusing for x-polarized light (XLP) is observed at $F = 60$ μm as indicated by the white dotted line in Fig. 7(a). The focal plane (zx) resides

Optical Materials EXPRESS

along the dotted line and Fig. 7(b) demonstrates the intensity profile of the focused light on the plane. Figure 7(c)-d exhibit the normalized intensity with full-width at half-maximum (FWHM) of the transmitted light along the primary orthogonal diameters of the metalens: the x and the z-axis, signifying intense optical focusing. The theoretically estimated FWHM is $\frac{0.514\lambda}{NA}$ (= 4.11 μm), where NA is the numerical aperture (= $\sin[\tan^{-1}(D/2F)]$, if surrounded by air). Thus, this design validates near-diffraction-limited focusing at 2 μm waveband. To analyze the ON-OFF switching capability of the metalens, we have simulated the structure with cIST and found barely any focusing at the focal plane as displayed in Fig. 6(e)-f. This is expected as mentioned earlier that when aIST is transformed to cIST by joule heating, the entire structure becomes highly reflective for 2 μm waveband resulting in low transmittance.

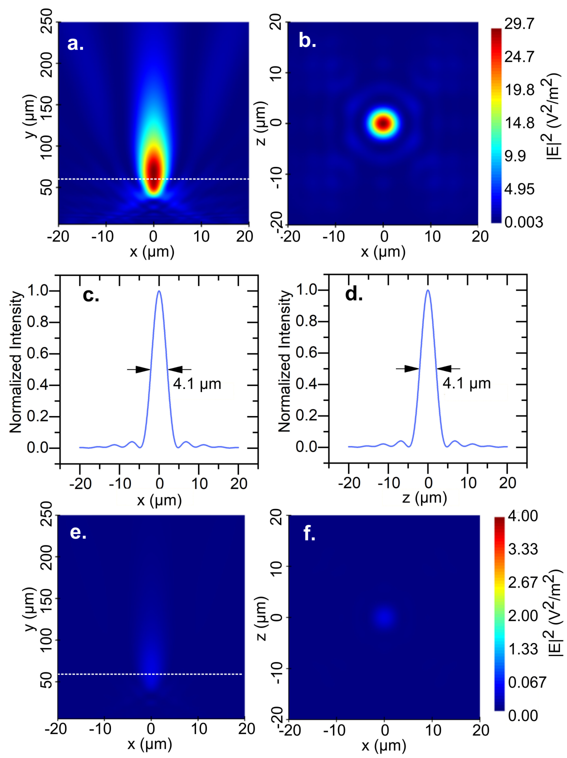

Fig. 7. Intensity profile for the focused x-polarized light beam during ON state along (a) xy plane (dotted line denotes the focal plane) and (b) zx plane. Normalized intensity of the focused beam with FWHM along (c) x-axis and (d) z-axis, manifesting a beyond diffraction-limited focusing. Intensity profile of the transmitted beam during the OFF state of the device along (e) xy plane (dotted line denotes the focal plane) and (f) zx plane, showing negligible focusing.

We have investigated the polarization insensitivity of the metalens by analyzing the focusing characteristics for linearly and circularly polarized light. As shown in Fig. 8(a)-d, the lens demonstrates similar focusing for LP (x-polarized: XLP and z-polarized: ZLP), RCP, and LCP light. Despite having optical absorption in materials and back reflection during the ON state, we have achieved ~ 76% focusing efficiency which is defined as the fraction of the incident optical power being concentrated within a radius of 1.5× FWHM on the focal plane around the focal axis (y) [58]. We have achieved an identical FWHM of 4.1 μm for XLP and ZLP ligh shown in Fig. 8(e)-f. From Fig. 8(g)-h, the FWHM is 3.48 μm for LCP and RCP light. Due to more symmetrical field distribution, the CP light has a narrower focal spot [59]. For the OFF state in

Optical Materials EXPRESS

Fig. 7(i)-l, the structure is highly reflective independent of the polarization of the incident light and inhibits focusing at the focal point. The ON-OFF switching ratio is 26 dB, defined by the ratio of the intensity of the focused light during the ON state to the OFF state. Adding more SiO_2-IST-ITO trilayers can further improve this performance while compromising the energy budget.

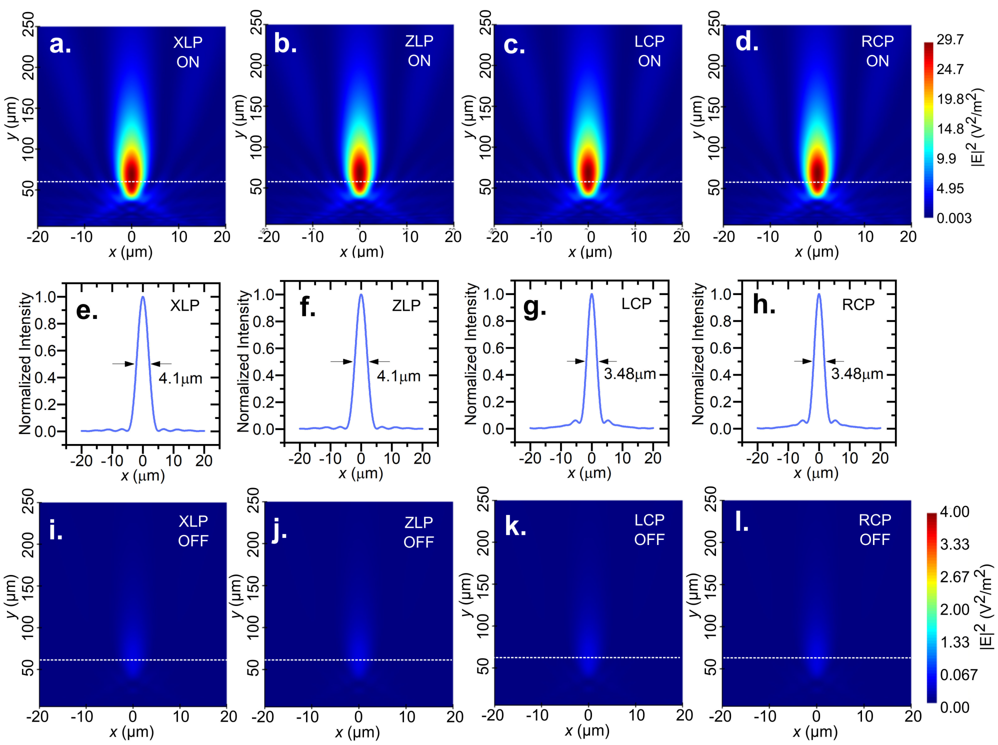

Fig. 8. Intensity profile for the focused (a) XLP, (b) ZLP, (c) LCP, and (d) RCP light beam during ON state along xy plane (dotted line denotes the focal plane). Normalized intensity of the focused beam with FWHM along the x-axis for (e) XLP, (f) ZLP, (g) LCP, and (h) RCP light. Intensity profile of the transmitted beam during the OFF state of the device along xy plane (dotted line denotes the focal plane) for (i) XLP, (j) ZLP, (k) LCP, and (l) RCP light, depicting trivial focusing.

Table 3 compiles some recently reported experimental and numerical studies similar to our multifunctional device for performance comparison. While most of the devices operate under the illumination of LP light, our proposed artifice shows excellent or similar performance for both LP and LCP/RCP lights. While absorption-transmission-based ON-OFF metadevices may encounter heating issues during their absorption state, as reported in [62] for 2D focusing, our design demonstrates 3D focusing with negligible absorption during the OFF state. Furthermore, in GSST [14] and Sb_2Se_3 [49] based lenses defocusing is accomplished by altering the devices' focal point by phase transition of the PCMs. Because of optical absorption in crystalline PCMs, the focusing efficiency diminishes notably. Furthermore, using a thick PCM layer to modulate the intensity of transmitted light demands higher electrical energy for effective switching [60]. In contrast, our proposed methodology surpasses the focal efficiency of existing devices by a profound margin and provides a scalable switching performance while consuming low switching energy. Thus, this reconfigurable metasurface will become a paradigm in multifunctional optics

Optical Materials EXPRESS

due to its noteworthy characteristics of polarization insensitivity, non-volatility, and low optical loss combined with dynamic electrical control over switching for point-of-care applications.

Table 3. Performance comparison of the proposed metastructure with recently reported metalenses

Device (Exp./Num.)[a]	Switching Method (Energy)	Operating Wavelength	Polarization	Focal Efficiency	Switching Ratio
(Exp.) SiN_x nanohole atop GSST [60]	Electical (2.3 × 10^5 nJ/μm^2)	1.43-2 μm	LP	-	5.5 dB
(Exp.) GST ring on Si [61]	Optical and annealing	400 μm	LP	-	4.77 dB
(Exp.) Sb_2Se_3 nanopillar on ITO [49]	Electrical	1.55 μm	-	-	28.7 dB
(Exp.) Geometric structures of GSST [14]	Annealing	5.2 μm	LP	23.7%	29.5 dB
(Num.) VO_2 buried in SiC [62]	-	678-795 nm	LP	30.57%	21.1 dB
This work	Electrical (232.98 nJ/μm^2)	2 μm	LP and CP	76%	26 dB

[a]Exp. - experimental study, Num. - numerical study

4. Conclusion

This study introduces a dynamically tunable metalens operating at 2 μm communication waveband, a standard for future communication technologies. The integration of the IST and the ITO micro-heaters resulted in efficient multi-level switching with an optimized modulation depth of 80% consuming 232.98 nJ/μm^2 switching energy, marking a significant advancement in tunable optical devices. The high focusing efficiency of 76% and a robust 26 dB switching ratio highlight the device's potential for mitigating optical signal dispersion and distortion. The polarization insensitivity and multi-level transmission functionalities with electrical control enhance its applicability in a range of optical environments, from telecommunication to memory applications. Thus, this work not only advances metasurface technology but also provides a framework for designing adaptable, high-performance optical systems capable of meeting future data transmission demands.

Funding. Research and Innovation Center for Science and Engineering (RISE), Bangladesh University of Engineering and Technology (BUET) (IRG Application ID 2023-02-006).

Acknowledgement. DSMC acknowledges support of Internal Research Grant (Application ID 2023-02-006) by Research and Innovation Center for Science and Engineering (RISE), Bangladesh University of Engineering and Technology (BUET).

Disclosures. The authors declare no conflicts of interest.

Data availability. Data underlying the results presented in this paper are not publicly available at this time but may be obtained from the authors upon reasonable request.

References

1. D. J. Richardson, "Filling the light pipe," Science **330**(6002), 327–328 (2010).
2. P. Boncz, T. Neumann, and V. Leis, "FSST," Proc. VLDB Endow. **13**(12), 2649–2661 (2020).
3. M. P. Ninos, P. Mukherjee, C. Psomas, *et al.*, "Full-duplex df relaying with parallel hybrid fso/rf transmissions," IEEE Open J. Commun. Soc. **2**, 2502–2515 (2021).
4. D. Kong, Y. Liu, Z. Ren, *et al.*, "Super-broadband on-chip continuous spectral translation unlocking coherent optical communications beyond conventional telecom bands," Nat. Commun. **13**(1), 4139 (2022).

5. P. J. Roberts, F. Couny, H. Sabert, *et al.*, "Ultimate low loss of hollow-core photonic crystal fibres," Opt. Express **13**(1), 236 (2005).
6. E. Russell, F. Gunning, K. Shortiss, *et al.*, "Development of thulium-doped fibre amplifiers for the 2µm waveband," in *Fiber Lasers and Glass Photonics: Materials through Applications*, S. Taccheo, M. Ferrari, J. I. Mackenzie, *et al.*, eds. (SPIE, 2018), p. 97.
7. K. Scholle, S. Lamrini, P. Koopmann, *et al.*, *2 µm Laser Sources and Their Possible Applications* (InTech, 2010), chap. 21.
8. W. Cao, D. Hagan, D. J. Thomson, *et al.*, "High-speed silicon modulators for the 2μm wavelength band," Optica **5**(9), 1055 (2018).
9. M. A. H. Bhuiyan, S. A. Mitu, and S. M. Choudhury, "TiN-GST-TiN all-optical reflection modulator for the 2μm wave band reaching 85% efficiency," Appl. Opt. **61**(31), 9262 (2022).
10. Q. Zhao, W. Yuan, J. Qu, *et al.*, "Optical fiber-integrated metasurfaces: An emerging platform for multiple optical applications," Nanomaterials **12**(5), 793 (2022).
11. Y. Li, J. Xie, L. Deng, *et al.*, "Active metasurfaces based on phase transition material vanadium dioxide," Sci. China Mater. **66**(1), 284–290 (2023).
12. C. Zhang, F. Yue, D. Wen, *et al.*, "Multichannel metasurface for simultaneous control of holograms and twisted light beams," ACS Photonics **4**(8), 1906–1912 (2017).
13. C. Spägele, M. Tamagnone, D. Kazakov, *et al.*, "Multifunctional wide-angle optics and lasing based on supercell metasurfaces," Nat. Commun. **12**(1), 3787 (2021).
14. M. Y. Shalaginov, S. An, Y. Zhang, *et al.*, "Reconfigurable all-dielectric metalens with diffraction-limited performance," Nat. Commun. **12**(1), 1225 (2021).
15. Y. Li, J. Luo, X. Li, *et al.*, "Switchable quarter-wave plate and half-wave plate based on phase-change metasurface," IEEE Photonics J. **12**(2), 1–10 (2020).
16. Y. Meng, T. Cao, and Y. Long, "Progress in metasurfaces based on Ge-Sb-Te phase-change materials," J. Appl. Phys. **128**(14), 140904 (2020).
17. I. A. Oliveira, I. L. G. de Souza, and V. F. Rodriguez-Esquerre, "Design of hybrid narrow-band plasmonic absorber based on chalcogenide phase change material in the infrared spectrum," Sci. Rep. **11**(1), 21919 (2021).
18. S.-J. Kim, I. Kim, S. Choi, *et al.*, "Reconfigurable all-dielectric fano metasurfaces for strong full-space intensity modulation of visible light," Nanoscale Horiz. **5**(7), 1088–1095 (2020).
19. S. Tao, Q. Li, J. Wang, *et al.*, "Phase change materials for nonvolatile, solid-state reflective displays: From new structural design rules to enhanced color changing performance," Adv. Opt. Mater. **8**(10), 2000062 (2020).
20. P. Fantini, "Phase change memory applications: the history, the present and the future," J. Phys. D: Appl. Phys. **53**(28), 283002 (2020).
21. X. Jiang, Q. Luo, H. Yuan, *et al.*, "Light-manipulated phase change materials for multi-functional thermal camouflage," in *Third International Computing Imaging Conference (CITA 2023)*, X. Shao, ed. (International Society for Optics and Photonics, 2023), p. 228.
22. T. Cao, X. Zhang, W. Dong, *et al.*, "Tuneable thermal emission using chalcogenide metasurface," Adv. Opt. Mater. **6**(16), 1800169 (2018).
23. T. Singh and R. R. Mansour, "Loss compensated pcm gete-based latching wideband 3-bit switched true-time-delay phase shifters for mmwave phased arrays," IEEE Trans. Microwave Theory Tech. **68**(9), 3745–3755 (2020).
24. S. Wintersteller, O. Yarema, D. Kumaar, *et al.*, "Unravelling the amorphous structure and crystallization mechanism of gete phase change memory materials," Nat. Commun. **15**(1), 1011 (2024).
25. R. Zhao, M. He, L. Wang, *et al.*, "Improved multilevel storage capacity in $Ge_2Sb_2Te_5$-based phase-change memory using a high-aspect-ratio lateral structure," Sci. China Mater. **65**(10), 2818–2825 (2022).
26. S. Zhang, X. Chen, K. Liu, *et al.*, "Nonvolatile reconfigurable terahertz wave modulator," PhotoniX **3**(1), 7–14 (2022).
27. S. Mohammadi-Pouyan, S. Bahadori-Haghighi, A. Rafatmah, *et al.*, "Design and analysis of nonvolatile GSST-based modulator utilizing engineered mach-zehnder structure with graphene heaters," Opt. Laser Technol. **169**, 110088 (2024).
28. A. Mahmoodi, M. Miri, M. H. Sheikhi, *et al.*, "GeSbSeTe-based high extinction ratio optical modulator," Appl. Opt. **62**(11), 2776 (2023).
29. B. Liu, W. Liu, Z. Li, *et al.*, "Y-doped Sb_2Te_3 phase-change materials: Toward a universal memory," ACS Appl. Mater. Interfaces **12**(18), 20672–20679 (2020).
30. H. Wang, J. Ye, H. Kang, *et al.*, "Sb_2Te_3/MoS_2 heterojunction photodetector for broadband light detection ranging from visible to near-infrared wavelengths," AI and Optical Data Sciences V **12903**, 41–131 (2024).
31. H. Chen, T. Wang, J. Yang, *et al.*, "Ultra-compact Sb_2Te_3-Silicon hybrid integrated arbitrarily cascaded tunable mode converter," IEEE Photonics J. **14**(2), 1–7 (2022).
32. L. Lu, S. F. Reniers, Y. Wang, *et al.*, "Reconfigurable InP waveguide components using the Sb_2Te_3 phase change material," J. Opt. **24**(9), 094001 (2022).
33. M. Delaney, I. Zeimpekis, H. Du, *et al.*, "Nonvolatile programmable silicon photonics using an ultralow-loss Sb_2Te_3 phase change material," Sci. Adv. **7**(25), eabg3500 (2021).
34. Q. Zhang and Y. Lu, "Tunable optical power splitter based on directional coupler structure with phase change material Sb_2Te_3," Opt. Commun. **554**, 130130 (2024).

35. S. Zhou, S. Zhou, S. Zhou, *et al.*, "Continuous programmable mid-infrared thermal emitter and camouflage based on the phase-change material In_3SbTe_2," Opt. Lett. **48**(16), 4388–4391 (2023).
36. M. A. H. Bhuiyan, S. A. Mitu, and S. M. Choudhury, "VO $_2$-based all-optical reflection modulator for 2μm wave band," in *2023 IEEE Photonics Conference (IPC)*, (IEEE, 2023), pp.1–2.
37. A. Zhao, X. Xiao, Z. T. Hu, *et al.*, "Multifunctional f-doped TiO_2 PCM microcapsules for visible-light-driven photocatalysis and latent heat storage," Appl. Energy **359**, 122674 (2024).
38. B. Lu, Y. Zhang, J. Zhang, *et al.*, "Preparation, optimization and thermal characterization of paraffin/nano-Fe_3O_4 composite phase change material for solar thermal energy storage," Journal of Energy Storage **46**, 103928 (2022).
39. M. S. Irshad, N. Arshad, J. Zhang, *et al.*, "Wormlike perovskite oxide coupled with phase?change material for all?weather solar evaporation and thermal storage applications," Adv. Energy Sustainability Res. **4**(3), 103928 (2023).
40. O. Novodvorsky, L. Parshina, O. Khramova, *et al.*, "Laser synthesis of volatile memristors based on niobium oxide thin films," Surf. Interfaces **30**, 101891 (2022).
41. J. K. Kana, G. Vignaud, A. Gibaud, *et al.*, "Thermally driven sign switch of static dielectric constant of VO_2 thin film," Opt. Mater. **54**, 165–169 (2016).
42. A. Heßler, S. Wahl, T. Leuteritz, *et al.*, "In_3SbTe_2 as a programmable nanophotonics material platform for the infrared," Nat. Commun. **12**(1), 924 (2021).
43. L. Conrads, N. Honné, A. Ulm, *et al.*, "Reconfigurable and polarization?dependent grating absorber for large?area emissivity control based on the plasmonic phase?change material In_3SbTe_2," Adv. Opt. Mater. **11**(8), 2202696 (2023).
44. C. Meng, Y. Zeng, D. Lu, *et al.*, "Broadband hyperbolic thermal metasurfaces based on the plasmonic phase-change material In_3SbTe_2," Nanoscale **15**(13), 6306–6312 (2023).
45. D. Lu, Y. Zeng, Q. Yan, *et al.*, "Tunable hyperbolic polaritons with plasmonic phase-change material In_3SbTe_2," Nanophotonics **13**(6), 937–944 (2024).
46. L. Conrads, L. Schüler, K. G. Wirth, *et al.*, "Direct programming of confined surface phonon polariton resonators with the plasmonic phase-change material In_3SbTe_2," Nat. Commun. **15**(1), 3472 (2024).
47. L. Conrads, F. Bontke, A. Mathwieser, *et al.*, "Infrared beam-shaping on demand via tailored geometric phase metasurfaces employing the plasmonic phase-change material In_3SbTe_2," (2024).
48. M. Wang, J. S. Lee, S. Aggarwal, *et al.*, "Varifocal metalens using tunable and ultralow?loss dielectrics," Adv. Sci. **10**(6), 2204899 (2023).
49. J. ye, C. Shen, H. Wang, *et al.*, "The phase-change-material-based dynamic metalens with ITO heater," in *High Contrast Metastructures XIII*, C. J. Chang-Hasnai, W. Zhou, H. Wang, and A. Alú, eds. (SPIE, 2024), p. 37.
50. M. N. Polyanskiy, "Refractiveindex.info database of optical constants," Sci. Data **11**(1), 94 (2024).
51. S. Abdollahramezani, O. Hemmatyar, M. Taghinejad, *et al.*, "Electrically driven reprogrammable phase-change metasurface reaching 80% efficiency," Nat. Commun. **13**(1), 1696 (2022).
52. I. D. Villar, C. Zamarreno, M. Hernaez, *et al.*, "Lossy mode resonance generation with Indium-Tin-Oxide-coated optical fibers for sensing applications," J. Lightwave Technol. **28**(1), 111–117 (2010).
53. G. M. Mangalgiri, P. Manley, W. Riedel, *et al.*, "Dielectric nanorod scattering and its influence on material interfaces," Sci. Rep. **7**(1), 4311 (2017).
54. L. Wang, J. Wen, C. Yang, *et al.*, "Potential of ITO thin film for electrical probe memory applications," Sci. Technol. Adv. Mater. **19**(1), 791–801 (2018).
55. H. T. Nguyen, A. Kusiak, J. L. Battaglia, *et al.*, "Thermal properties of In-Sb-Te thin films for phase change memory application," in *6th Forum on New Materials - Part C*, (2014), p. 113–119.
56. W. Zhu, G. Zheng, S. Cao, *et al.*, "Thermal conductivity of amorphous SiO_2 thin film: A molecular dynamics study," Sci. Rep. **8**(1), 10537 (2018).
57. T. Ashida, A. Miyamura, N. Oka, *et al.*, "Thermal transport properties of polycrystalline Tin-doped Indium Oxide films," J. Appl. Phys. **105**(7), 073709 (2009).
58. S. Banerji, M. Meem, A. Majumder, *et al.*, "Imaging with flat optics: metalenses or diffractive lenses?" Optica **6**(6), 805 (2019).
59. B. Richards and E. Wolf, "Electromagnetic diffraction in optical systems, ii. structure of the image field in an aplanatic system," Proc. R. Soc. Lond. A **253**(1274), 358–379 (1959).
60. C. C. Popescu, K. Aryana, P. Garud, *et al.*, "Electrically reconfigurable phase-change transmissive metasurface," Adv. Mater. **36**, 2400627 (2024).
61. X. Chen, S. Zhang, K. Liu, *et al.*, "Reconfigurable and nonvolatile terahertz lithography-free photonic devices based on phase change films," Photonics Res. **11**(4), 669 (2023).
62. M. E. Karim and S. M. Choudhury, "Reconfigurable broadband metasurface with switchable functionalities in the visible range," Opt. Mater. Express **13**(5), 1409 (2023).